ISSN 1330-3651 (Print), ISSN 1848-6339 (Online)
https://doi.org/10.17559/TV-20241024002088
Original scientific paper

Innovative Eye-Tracking Technology Using Angled Comb Drive MEMS Mirrors: A Computational and Experimental Analysis

YanTing XIA, Qian WANG, Qitao LI*, Lin ZHANG

Abstract: Eye-tracking technology captures eye movement and gaze point information by leveraging the characteristics of the human eye, using hardware devices in combination with software algorithms. It is a cutting-edge technique that can shorten the process of human-computer interaction. MEMS (Micro-Electro-Mechanical Systems) mirrors, with their low power consumption, high precision, and fast response times, can ensure the accuracy and speed required for eye tracking. In this paper, we propose an innovative design of angled comb fingers based on the traditional comb drive structure for electrostatic MEMS mirrors. Through steady-state simulations and numerical calculations, we analyze the relationships between beam length, beam width, mirror size, and resonant frequency. We also calculate the parameter relationships for traditional, serpentine, and angled comb drives. The maximum displacement generated by the oblique comb electrostatic micromirror designed in this paper is 5.18×10^{-4} μm, which is 3.3 times of the approximate normal comb displacement and 4.6 times of the serpentine comb displacement. Based on the scanning characteristics of electrostatic MEMS mirrors, we establish a relationship model between eye movement angle and the interval of signal peaks using geometric modeling, demonstrating a nonlinear relationship influenced by trigonometric functions. Finally, by combining theoretical and experimental methods, we discovered that the signals obtained from left and right eye movements are nearly symmetrical with respect to the 0° position. The peak spacing error brings the error value of the eye-movement angle measurement to be less than 0.1°, and the experimental system achieved an eye-tracking accuracy of better than 1°. Therefore, this research provides a theoretical foundation and methodological guidance for the broad application of electrostatic MEMS mirrors in the field of eye tracking.

Keywords: electrostatic comb drives; eye tracking; experimental analysis; mems mirrors; numerical calculation

1 INTRODUCTION

In recent years, the global surge of interest in the metaverse has prompted major companies to launch mixed reality devices that enable interaction between virtual and real worlds. Eye-tracking technology serves as one of the key bridges for facilitating such interactions and has become a research focus for numerous academic institutions and tech companies [1]. Moreover, eye-tracking allows for high-resolution imaging in areas where the user is looking, while maintaining low-resolution imaging in peripheral areas, significantly reducing GPU load and improving device performance [2]. In the medical field, eye-tracking technology can be applied in the screening and treatment of ophthalmic and psychiatric disorders, such as strabismus, autism, and Alzheimer's disease [3-6]. This demonstrates the immense application value and promising development prospects of eye-tracking technology.

In general, the driving mechanisms for MEMS mirrors can be categorized into four major types: electrostatic drive [7], piezoelectric drive [8], electrothermal drive [9], and electromagnetic drive [10]. Electrostatic MEMS mirrors, due to their relatively simple structure, lower manufacturing costs, and reduced complexity, along with features such as low power consumption and fast response times, are widely used in fields like VR/AR and visual imaging. MEMS mirrors are optical devices in which a microactuator drives a micromirror, allowing the assembly of the mirror, actuator, and laser-emitting device to achieve laser beam deflection, graphical scanning, or image display [11]. He et al. [12] designed a two-dimensional electrostatic MEMS mirror with dimensions of 3.3 × 3.3 mm, featuring mechanical scan angles of ±1.5° for both fast and slow axes. The uniqueness of this mirror lies in its use of repulsive electrostatic force. However, the overall optical scanning angle of this mirror is relatively small, making it difficult to achieve large field-of-view scanning. Ko et al. [13] designed a novel electrostatic scanning mirror with a circular mirror surface and an elliptical frame with vertical comb drives. To increase driving force, stationary vertical comb electrodes were positioned both above and below the movable combs, but this increased the design cost and manufacturing complexity. Milanovic et al. [14] developed a frameless 2D electrostatic MEMS mirror with a mirror diameter of 0.8mm and scan angle of 16° for all axes, though the small mirror size limited the achievement of larger scan angles. Liu et al. [15] proposed a MEMS mirror with both fast and slow axes using planar comb structures. This mirror was fabricated with an improved isolated trench wiring method, enhancing device reliability and mechanical stability, but its scan angle was limited to within 10°.

The application of recording eye movements has been demonstrated in various fields. Early methods relied on direct observation and mechanical recording to capture eye movements in a simple manner [16]. Tsinghua University's Ding team proposed an improved algorithm framework for achieving single or dual-eye tracking and eye contour parameter extraction [17]. The method relies strictly on the optimized algorithm to accomplish the extraction of eye contour parameters, and the robustness and accuracy of the algorithm itself are not described in detail. Zhang from Wuhan University of Technology developed an eye tracking-learning-detection algorithm with feedback, addressing current challenges such as eye occlusion, morphological changes, and scale variation, thereby improving accuracy [18]. However, it does not have an integrated evaluation of the overall eye tracking, and the accuracy of the implementation is only dependent on the algorithm to achieve, so it is difficult to make a judgment in the actual application due to the error brought by the hardware system. Internationally, Japanese researcher Yamamoto successfully reduced the computational load of the system by limiting the scanning area in eye-tracking, while maintaining sufficient accuracy [19]. But the method sacrifices the scanning area of the eye tracking itself, and for different people, whose eye contours are not consistent in shape and size, it is desirable to achieve as much accuracy as possible without losing the scanning area. Amudha applied a genetic algorithm, achieving up to 98% positioning accuracy in a short period [20]. Nevertheless, the proposed genetic algorithm requires a large number of samples to be solved and may fall into local optimal solutions, resulting in failure to obtain the global optimal solution. Although infrared camera-based eye-tracking systems have been extensively researched and are technologically mature, there is an urgent need for a new approach to optimize and replace them due to the trade-offs between camera performance, image processing capability, and device size. With the rapid development of MEMS technology, the eye tracking system based on the dual modality of MEMS mirror and camera has become a research trend within foreign countries. D. Beymer et al. [21] designed a 3D eye-tracking system that allows for head movement without requiring markers or wearable devices, but it suffers from high power consumption and lack of portability, making it unsuitable for general use. Topal et al. [22] developed an eye-tracking method based on a glasses-like frame, utilizing multiple fixed light sources and light-reflecting sensors. However, this method imposes high algorithmic demands for eye tracking. Bobić et al. [23] proposed a camera-based eye-tracking technique that uses image segmentation to calculate the pupil's coordinates in each consecutive video frame, though the accuracy of this system is limited, with tracking errors mainly resulting from the camera's image processing limitations.

To address the challenges associated with MEMS mirrors and their applications in eye-tracking, this paper presents an innovative approach by proposing an angled comb drive structure for electrostatic MEMS mirrors and conducting a parametric analysis [24]. The relationships between beam length, beam width, mirror size, and resonant frequency were thoroughly examined. To solve the difficulties in signal capture for eye-tracking, a relationship model was established between eye movement angle and the interval of signal peaks, demonstrating a nonlinear relationship influenced by trigonometric functions. The feasibility and accuracy of the proposed method were verified through experiments. This research provides fundamental guidance and theoretical support for the broad application of electrostatic MEMS micromirrors in the field of eye-tracking.

2 METHOD
2.1 Lissajous Scanning of MEMS Micromirrors

MEMS electrostatic actuation uses electrostatic attraction as the driving force. It is highly effective over short distances and allows for precise control, but the electrostatic attraction diminishes rapidly as the distance increases [25]. The Lissajous scanning pattern generated by MEMS mirrors is derived from simple harmonic motion, where a particle undergoes harmonic motion in two mutually perpendicular directions, and the resultant motion forms a Lissajous figure. This pattern can be described using the following mathematical expression:

$$\begin{cases} x_t = A_x \sin(2\pi \cdot f_x \cdot t_i + \varphi_x) \\ y_t = A_y \sin(2\pi \cdot f_y \cdot t_i + \varphi_y) \end{cases} \tag{1}$$

In the equation, A_x and A_y represent the amplitudes, f_x and f_y are the frequencies, t is time, and φ represents the phase. If the ratio of the two frequencies is a rational number, the resulting Lissajous scanning pattern forms a stable, closed curve. However, if the frequency ratio is irrational, the pattern will densely fill the entire display area. Additionally, the appearance of the Lissajous figure changes with variations in the phase φ, as shown in Fig. 1.

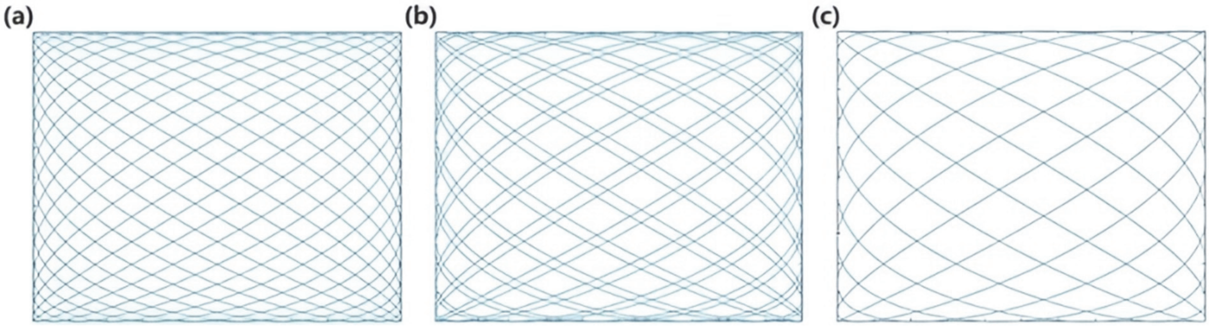

Figure 1 Relationship between Risaru's graphical style and initial phase (a) initial phase of 0°; (b) initial phase of 90°; (c) initial phase of 180°

The application and significance of Lissajous figures in engineering lie in their ability to serve as an analytical and visualization tool, helping engineers and scientists understand signal characteristics, vibration modes, sound wave interference, and the stability of control systems. Electrostatic MEMS mirrors exhibit good frequency stability, ensuring that the vibration frequency of each axis remains constant. Leveraging this characteristic, the mirrors can achieve stable single-axis or dual-axis harmonic oscillations. The scanning process of MEMS mirrors can be expressed mathematically and the angular displacement of single-axis harmonic oscillation for the mirror follows the equation:

$$\theta = \theta_m \cdot \sin\left(\omega t\right) \tag{2}$$

In this equation, θ_m represents the specified maximum vibration angle, w is the angular frequency of vibration, and t is time. The vibration directions of the two axes of the MEMS mirror are perpendicular to each other, establishing a rectangular coordinate system. The maximum vibration angles for the two axes are θ_{mx} and θ_{my}, while the angular frequencies are w_x and w_y, with the corresponding angular displacements being θ_x and θ_y. The center of the mirror is denoted as O', and the origin of the Cartesian coordinate system is O. Through mathematical derivation, the position coordinates corresponding to the reflected light rays, $x = L \cdot \tan\theta_x$ and $y = L \cdot \tan\theta_y$, can be obtained. By substituting the formula for single-axis harmonic vibration of the mirror, we get:

$$\begin{cases} x = L \cdot \tan\left(\theta_{mx} \cdot \sin\left(\omega_x t\right)\right) \approx L \cdot \tan\theta_{mx} \cdot \sin\left(\omega_x t\right) \\ y = L \cdot \tan\left(\theta_{my} \cdot \sin\left(\omega_y t\right)\right) \approx L \cdot \tan\theta_{my} \cdot \sin\left(\omega_y t\right) \end{cases} \tag{3}$$

Let: $L \cdot \tan\theta_{mx} = x_0$, $L \cdot \tan\theta_{my} = y_0$, then there are:

$$\begin{cases} x = x_0 \cdot \sin\left(\omega_x t\right) \\ y = y_0 \cdot \sin\left(\omega_y t\right) \end{cases} \tag{4}$$

Considering $\omega_x = 2\pi f_x$ and $\omega_y = 2\pi f_y$, substituting these values into the calculation yields: $x = x_0 \cdot \sin\left(2\pi f_x t\right)$ and $y = y_0 \cdot \sin\left(2\pi f_y t\right)$. Here, f_x represents the frequency of the harmonic oscillation of the scanning spot formed by the MEMS mirror in the direction parallel to the axis, while f_y denotes the frequency of the harmonic oscillation in the axial direction. When the initial phase is set to zero, the following applies:

$$\frac{f_x}{f_y} = \frac{\sin^{-1}\dfrac{x}{x_0}}{\sin^{-1}\dfrac{y}{y_0}} \tag{5}$$

The equation shows that the scanning through the MEMS galvanometer is a Lissajous scan, and when the ratio of the frequencies of the two axes of the galvanometer's simple harmonic oscillations is kept constant, the scanning line constitutes a Lissajous pattern.

2.2 Static Comb Structure Design

When a driving voltage is applied, the mirror torsion occurs, which can usually be approximated as a mass rotating about a central axis under the action of a driving force, and can be represented by a second-order oscillatory system:

$$I\frac{d^2\theta}{dt^2} + b\frac{d\theta}{dt} + K\theta = M(\theta) \tag{6}$$

θ is the deflection angle, b is the air damping coefficient, K is the elasticity coefficient of the beam, I is the rotational inertia, and M is the applied torque. The torque of the electrostatic comb drive is:

$$M(\theta) = \frac{1}{2}(2N)\frac{\partial C}{\partial\theta}V^2 \tag{7}$$

N represents the number of comb finger pairs for the fast or slow axis, C is the capacitance between a single fixed comb finger and the movable comb finger, and V denotes the drive voltage. When the mirror twists, the capacitance varies with the angle, meaning that the torque provided by the electrostatic comb drive is influenced by both time and angle. For this second-order system, the twisting amplitude of the mirror reaches its maximum when the resonant frequency is half of the frequency of the applied excitation signal. Fig. 2a illustrates the novel serpentine comb mirror structure proposed in this paper, while the enlarged view of the comb structure is shown in the right panel Fig. 2b. By tilting the conventional comb fingers 45° in the same direction, a slanted comb structure is obtained. Compared to the conventional comb structure, the width, length, and spacing of the comb fingers remain unchanged, but the number of comb fingers is reduced. The horizontal direction represents the fast axis, and the vertical direction represents the slow axis. The movable comb fingers of the fast axis are directly connected to the mirror surface, while those of the slow axis are connected to the frame. The elastic beams are rectangular, with the fast axis beam connected to the mirror surface and the slow axis beam connected to the frame. The lengths and widths of the slow axis beams are both greater than those of the fast axis beams. The mirror surface dimensions and relevant parameters for the fast and slow axes of the slanted comb mirror are shown in Tab. 1. Compared to the conventional comb mirror, the mirror size, overall thickness, beam length, and beam width remain unchanged, with the mirror size being 800 μm and the overall thickness being 50 μm. Based on the overall dimensions and comb finger sizes, there are 24 pairs of fast axis comb fingers and 52 pairs of slow axis comb fingers, which is comparable to the number of comb fingers in the conventional comb mirror.

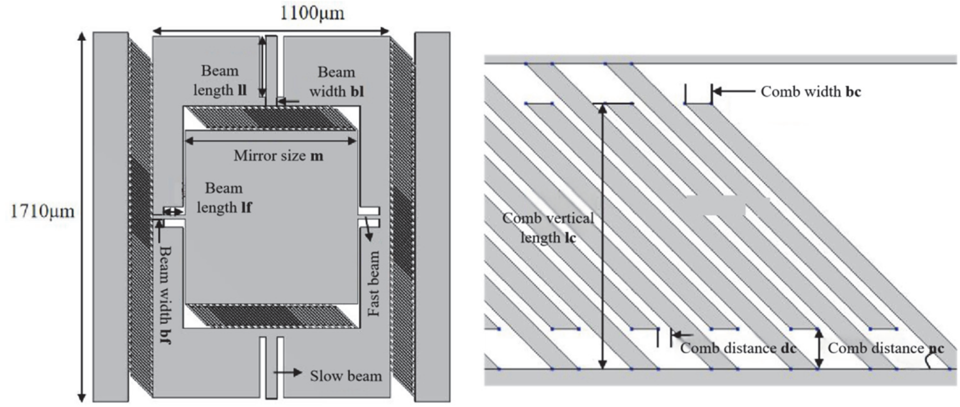

Figure 2 Design of electrostatic helical tooth structure (a) overall structure of oblique comb tooth vibrating mirror; (b) enlarged diagonal comb tooth structure

Table 1 Parameters related to micromirror design

Parametername	Parameter sizes	Parameter name	Parameter sizes
Mirror sizem	800 μm	Comb vertical lengthlc	100 μm
Fast-axis beam width bf	20 μm	Comb widthbc	10 μm
Fast-axis beam length lf	100 μm	Comb spacingdc	5 μm
Thicknesses hc	50 μm	Combing distancenc	15 μm
Slow-axis beam width bl	50 μm	Number of fast-axis comb pair sn1	24
Slow shaft beam length ll	280 μm	Number of pairs of slow shaft comb sn2	52

2.3 Parametric Calculation and Modal Analysis

Fig. 3 illustrates an electrostatic micro-mirror with a mirror size of 800 × 800 μm, comb finger length of 100 μm, comb finger width of 10 μm, comb finger spacing of 5 μm, mirror thickness of 50 μm, beam length of 100 μm, and beam width of 20 μm. Surrounding the mirror is a cubic air domain with a side length of 10,000 μm. The cell size for the mirror's various domains is refined, while the cell size for the air domain is coarsened. The cube is distributed in an 8-unit sweeping pattern, which simplifies the model's calculations and improves computational speed. The driving voltage for the fixed frame and fixed comb fingers (shown in blue in Fig. 3a) is set to 0 V, while the driving voltage for the mirror surface and movable comb fingers (shown in green in Fig. 3b) is set to 50 V. Based on the computational analysis, the maximum displacement generated by the designed slanted comb electrostatic micro-mirror is 5.18×10^{-4} μm.

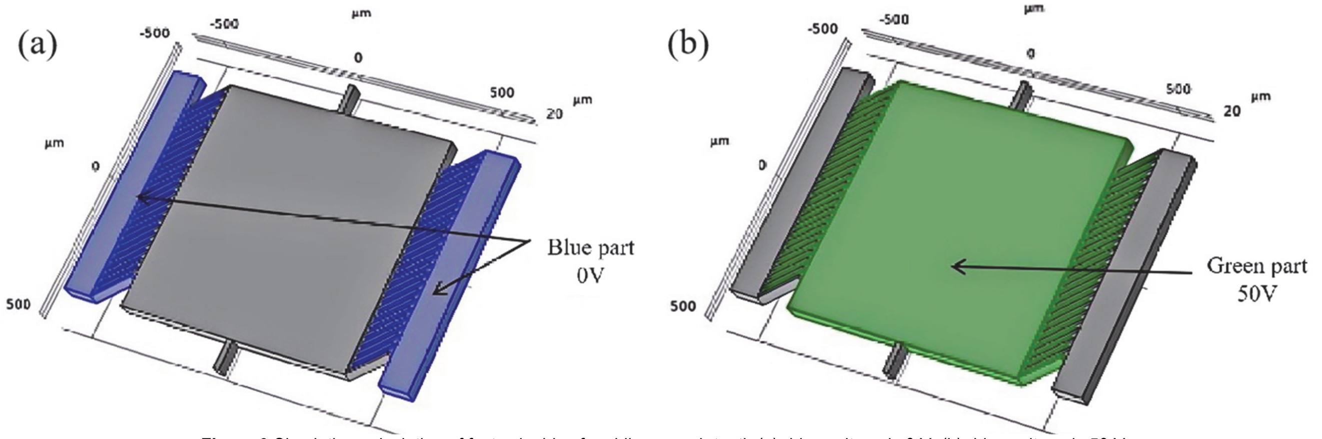

Figure 3 Simulation calculation of fast axis drive for oblique comb tooth (a) drive voltage is 0 V; (b) drive voltage is 50 V

To better analyze the comb structure presented in this study alongside other comb features, a parametric scan was conducted on the beam length, beam width, and mirror size of the MEMS mirror's fast axis for different electrostatic comb fingers, as shown in Fig. 4. The range for the beam length parametric scan was from 30 μm to 100 μm, the beam width ranged from 5 μm to 50 μm, and the mirror size varied from 800 μm to 1200 μm. Fig. 4a illustrates the relationship between beam length and resonant frequency for the three types of comb structures. It can be observed that beam length is inversely proportional to resonant frequency; as beam length increases, the resonant frequency decreases. Therefore, a larger beam length should be selected within an appropriate range. When the beam lengths are equal, the resonant frequencies of the ordinary and slanted comb fingers are similar, while the resonant frequency of the serpentine comb is consistently higher than the other two. Fig. 4b shows the relationship between beam width and fast-axis resonant frequency for the three comb structures. It is evident that beam width is directly proportional to resonant frequency; as beam width increases, resonant frequency also increases. In this case, a smaller beam width should be selected within an appropriate range, taking into account the allowable stress for the elastic beam in relation to both beam length and beam width. When the beam width ranges from 5 μm to 15 μm, the resonant frequencies for all three comb structures do not differ significantly. However, when the beam width exceeds 15 μm, the resonant frequencies of the ordinary and slanted combs remain relatively close, while the resonant frequency of the serpentine comb mirror is greater than those of the ordinary and slanted combs. When the beam widths are equal, the resonant frequencies of the ordinary and slanted combs are again similar, with the resonant frequency of the serpentine comb being higher. Fig. 4c depicts the relationship between mirror size and fast-axis resonant frequency for the three comb structures. Here, it is clear that mirror size is inversely proportional to resonant frequency; as mirror size increases, resonant frequency decreases. Within a suitable range, a larger mirror size should be selected. The rate of decrease in resonant frequency slows as the size increases. When the mirror sizes are equal, the resonant frequencies of the ordinary and slanted combs are comparable, while the resonant frequency of the serpentine comb is consistently higher, with the most significant difference at a mirror size of 800 μm and the least at 1200 μm. Fig. 4d presents the calculations of driving displacement for the ordinary, serpentine, and proposed slanted electrostatic comb fingers. The results indicate that the maximum displacement generated by the oblique comb electrostatic micromirror designed in this paper is 5.18×10^{-4}μm, which is 3.3 times of the approximate normal comb displacement and 4.6 times of the serpentine comb displacement. This highlights the promising performance and application potential of the newly proposed slanted comb micro-mirror.

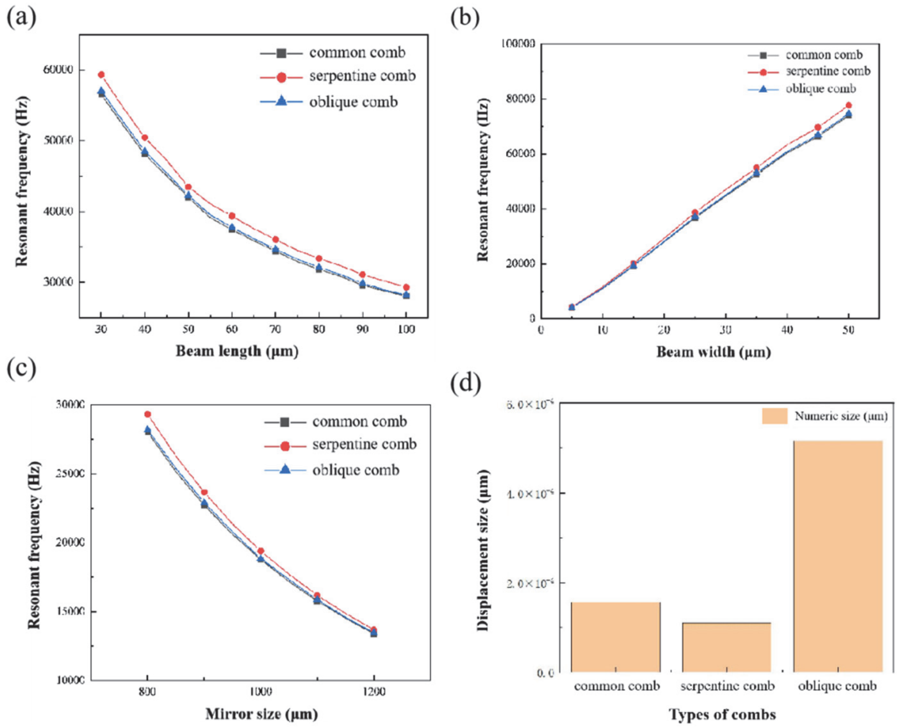

Figure 4 Parametric calculation and analysis of normal comb, serpentine comb and oblique comb (a) fast-axis resonance frequency versus fast-axis beam length; (b) fast-axis resonance frequency versus fast-axis beam width; (c) fast-axis resonance frequency versus galvanometer mirror size; (d) fringe displacement of the MEMS micromirror

2.4 Theoretical Approach to Eye Tracking

During the uniaxial scanning process of the MEMS mirror, the mirror performs high-precision harmonic vibrations along a single axis, causing the reflected light spot to sweep across a specific trajectory, thereby creating a one-dimensional scanning line segment. By finely adjusting the frequency of the excitation signal applied to the mirror, the length of the scanning line can be subtly modified to ensure it covers the entire surface of the eye. Additionally, by adjusting the relative positions of the hardware modules, the scanning line can be aligned to pass precisely through the center of the pupil, which is crucial for improving the accuracy of eye movement tracking. As shown in Figure 5, the scanning frequency of the MEMS mirror is fixed; therefore, when the eye rotates to different positions, the time interval between two crossings of the scanning line through the center of the cornea will vary. This change in time interval is induced by the movement of the eye and reflects the spatial displacement of the corneal center. During the scanning of the mirror, the principle of signal variation received by the photodiode is illustrated in Fig. 5a. By analyzing the differences in the time intervals of the signal peaks received by the photodiode, the specific position of the corneal center can be accurately determined. Utilizing this principle, Fig. 5b and Fig. 5c depict the characteristics of the peak light intensity of the reflected light rays corresponding to different positions of the eye during a complete scanning cycle. The eye-tracking system can track and record the eye's movement trajectory by analyzing the time intervals of the signal peaks received by the photodiode. This method generates changes in the photoelectric signals based on the differences in the reflection characteristics at various positions on the eye's surface, allowing the calculation of the eye's rotational angle.

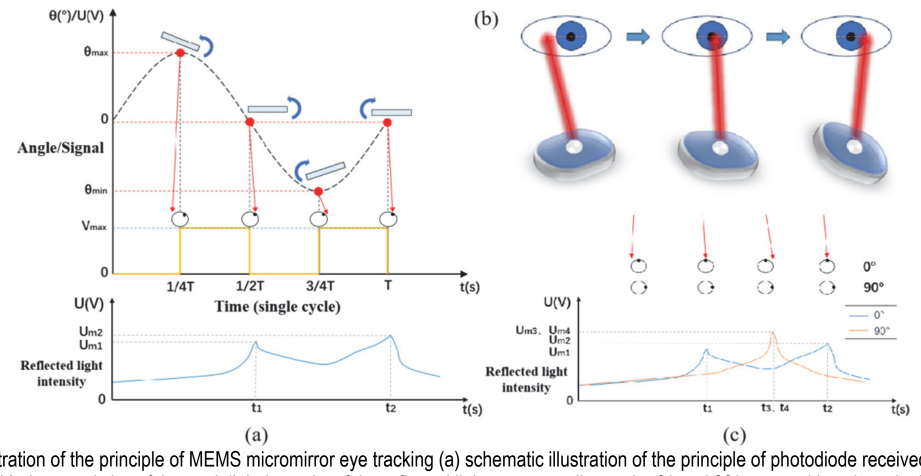

Figure 5 Schematic illustration of the principle of MEMS micromirror eye tracking (a) schematic illustration of the principle of photodiode received signal change when the mirror vibrates; (b) characteristics of the peak light intensity of the reflected light corresponding to the 0° and 90° eye positions in a single scanning cycle

2.5 Eye Tracking Scanning Discrimination Algorithm

In order to realize the goal of eye tracking more effectively, we can set T as the time corresponding to one scanning cycle of the galvanometer, t_1 and t_2 as the moments when the peaks appear under the 0° position, corresponding to the peaks U_{m1} and U_{m2}, and t_3 and t_4 as the moments when the peaks appear under the 90° position, corresponding to the peaks U_{m3} and U_{m4}. When the position of the eyeball is 0°, the peaks appear at intervals of half of the scanning cycle of the galvanometer:

$$t_2 - t_1 = \frac{T}{2} \tag{8}$$

When the eye position is 90°, the peak occurrence interval is 0. In order to find out the correspondence between the eye rotation angle and the peak interval time of the signal received by the photodiode, the theoretical derivation part establishes a two-dimensional right-angled coordinate system with the center of the eye as the origin, as shown in Fig. 6.

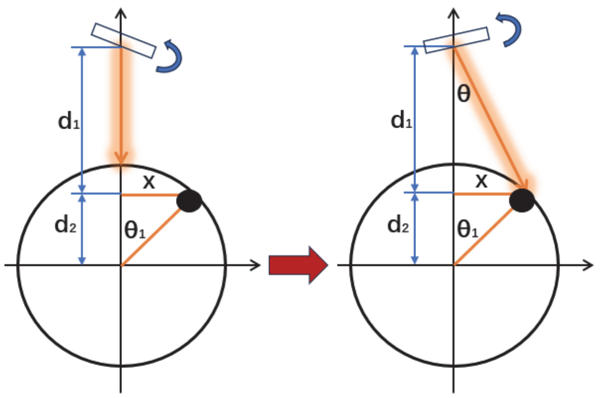

Figure 6 Geometric relationship between the scanning beam and the eyeball

where the black dot indicates the location of the corneal center, θ is the angular displacement generated by the scanning beam reflected under the simple harmonic vibration of the MEMS galvanometer, θ_1 is the angle of rotation of the eye, and d_1, d_2, and are the spacings of the corresponding positions. From the geometric relationship:

$$d_1 \cdot \tan\theta = d_2 \cdot \tan\theta_1 \tag{9}$$

and then get:

$$\theta_1 = \tan^{-1}\left(\frac{d_1}{d_2}\right) + \theta_m \cdot \sin(\omega t) \tag{10}$$

The time required for the scanning spot formed by the reflection of the MEMS galvanometer to reach the maximum scanning position for the first time from the axial position is $T/4$. Considering the symmetry of the scanning trajectory, the time interval Δt at which the symmetrical peaks appear at a given angle of rotation of the eye can be derived by using the two times of the difference between this time and t. This can be derived in turn:

$$\theta_1 = \tan^{-1}\left(\frac{d_1}{d_2}\right) + \theta_m \cdot \sin\left(\frac{\omega T}{4} - \frac{\omega \Delta t}{2}\right) \tag{11}$$

3 EXPERIMENTAL RESULTS AND DISCUSSION

3.1 Eye Tracking Experiment Test Platform Construction

To create a compact structure for the eye-tracking system, this study employs a zigzag layout for the optical path, allowing for the placement of as many system hardware modules as possible within a smaller space. This arrangement enables the laser beam to complete the scanning process through all modules over the shortest possible optical path, reducing light intensity loss and improving the overall signal-to-noise ratio of the system, thereby enhancing the accuracy of the measurement data. The proposed eye-tracking system based on the MEMS mirror is illustrated in Fig. 7a, which includes four core modules: the VCSEL laser, MEMS mirror, eyeball, and photodiode. The laser beam emitted by the eye-tracking system is reflected by the surface of the MEMS mirror, creating a scanning beam. This scanning beam is then reflected again from the surface of the eyeball, with the reflected light intensity being maximized when the scanning beam passes through the center of the cornea.

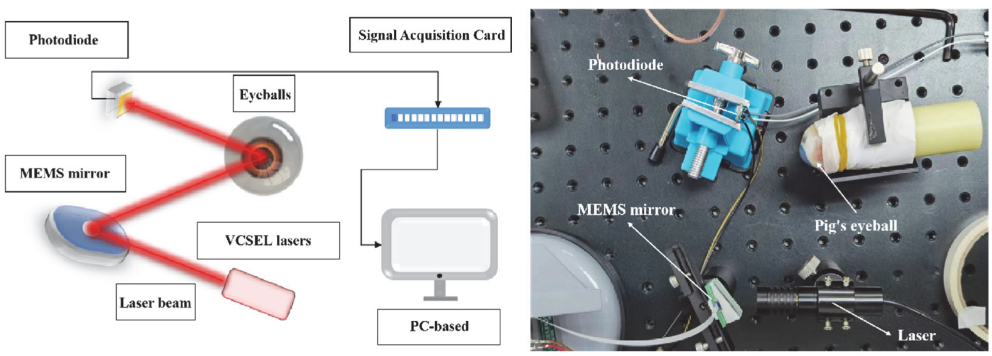

(a) (b)

Figure 7 Eye tracking experimental test system (a) schematic design of the experimental system building program; (b) schematic construction of the experimental setup of the eye tracking system

To facilitate quantitative analysis, an eye-tracking test platform was constructed, as shown in Fig. 7b, where a pig eyeball is fixed onto a rotating platform with scales. In order to reasonably control the variables and realize accurate analysis, when carrying out experimental measurements, ensure that the vibration of the micromirror is unchanged, rotate the corresponding angle on the rotator, yes the eyeballs according to the predetermined angle of offset, according to the different scanning angle, to determine the information of the point of light after reflecting through the MEMS micromirror.

3.2 Discussion and Analysis of Experimental Results

We take the two-dimensional MEMS electrostatic scanning mirror made by Beijing Institute of Technology as an example, its model is BIT-D3, the overall size of its micromirror is 10 × 7.9 mm, the diameter of the mirror is 3 mm, and the resonance frequency is 676 Hz at most. The electrostatic micromirror designed in this paper has a vibrating mirror drive signal frequency of up to 1050 Hz although the mirror size is smaller than that of the BIT-D3, and the frequency of the vibrating mirror drive signal is up to 1050 Hz, which can be achieved in the process of In the eye tracking scanning of micromirrors, the size of the resonant frequency directly determines the density of scanning and imaging accuracy, therefore, in the denseness level of scanning, high-frequency micromirrors are more superior. In the experiment, a graduated turntable was used to control the rotational angles of the pig eyeball, measuring eye-tracking test data from −10° to 10° with a gradient of 1°. A total of 21 data points were collected, with the data acquisition card continuously sampling data for each point. Considering the periodic nature of the scanning process, it is possible to calculate the number of discrete points captured by the acquisition card within a single scanning cycle based on the scanning frequency and sampling frequency, thereby enabling the analysis of eye movement characteristics within that cycle. As the angle of the eyeball changes, the characteristics of the peak values vary. The time intervals between the two symmetric peak values corresponding to each angle differ, which serves as the basis for determining eye movement angles and facilitating eye tracking. Let the sampling frequency of the acquisition card be f_s and the frequency of the mirror's harmonic motion be f, allowing us to calculate the number of sampling points n within one scanning cycle. In the experiment, the driving signal frequency of the mirror was set at 1050 Hz, resulting in a mirror vibration frequency of 525 Hz. The acquisition card used in the experiment had a sampling frequency of 25,000 Hz, leading to $n \approx 48$. For instance, with an eye movement angle of 10°, the raw signal captured after a single scanning cycle is shown in Fig. 8a. Within each cycle, the peaks are symmetrically distributed, and the time interval between the pair of highest amplitude peaks is defined as the peak interval Δt. To visually compare the peak characteristics in the raw data, the peak signals at 0° and 10° are presented together in Fig. 8b. From this comparison, it is observed that when the eye movement angle is 0°, the two symmetric main peaks are spaced far apart in time within a single scanning cycle; whereas, when the eye movement angle is 10°, the two symmetric main peaks are closer together in time. This analysis indicates that the trend of signal changes received by the photodiode is preliminarily consistent with the theoretical derivation of the eye-tracking judgment method discussed earlier.

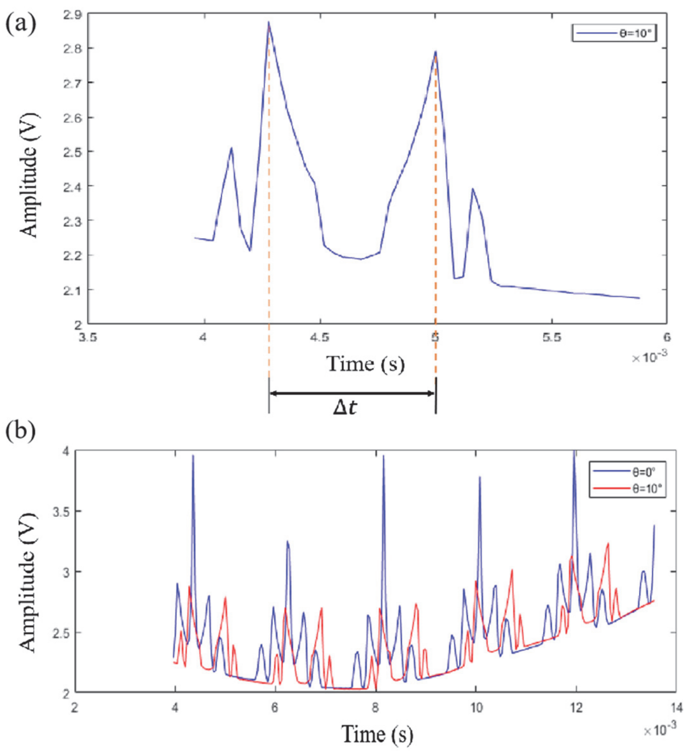

Figure 8 Signal processing and analysis at different scanning angles (a) raw signal corresponding to 10° eye movement angle after intercepting a single scanning cycle; (b) comparison of signal waveforms obtained from eye movement scans at 0° and 10°

To reduce the impact of 50 Hz power frequency interference and random factors, signals are processed over integer multiples of 20 ms. This involves calculating the sampling time interval, the period of the mirror's harmonic motion, and the least common multiple of these with 20 ms. The mean value of the time intervals of the symmetric peaks for each scanning cycle within this duration is computed. The calculations show that the time interval is 100 ms, and with a data acquisition card sampling frequency of 25,000 Hz, the number of sampling points needed is 2,500. Given that one scanning cycle of the mirror corresponds to approximately 48 sampling points, voltage data from 50 scanning cycles must be collected for each data point. After applying this processing to the data collected at all 21 angles, the voltage peak intervals captured by the photodiode for each eye movement angle are obtained. By plotting the data, a trend of how the peak intervals change with angle can be visualized, as shown in Fig. 9a. Considering that the experimental data exhibits a sinusoidal trend, a Fourier series fitting method is employed to derive the fitting curve using mathematical tools, as depicted in Fig. 9b.

Let the value of the eye movement angle be x and the value of the peak interval be y. The fitting relation is obtained as:

$$\begin{aligned} y &= a_0 + a_1 \cdot \cos(\omega x) + b_1 \cdot \sin(\omega x) + a_2 \cdot \cos(2\omega x) \\ &+ b_2 \cdot \sin(2\omega x) + a_3 \cdot \cos(3\omega x) + b_3 \cdot \sin(3\omega x) \\ &+ a_4 \cdot \cos(4\omega x) + b_4 \cdot \sin(4\omega x) + a_5 \cdot \cos(5\omega x) \\ &+ b_5 \cdot \sin(5\omega x) \end{aligned} \tag{12}$$

where $a_0 = 9.214 \times 10^{-4}$, $a_1 = 2.113 \times 10^{-5}$, $b_1 = 9.771 \times 10^{-5}$, $a_2 = 1.526 \times 10^{-4}$, $b_2 = 5.356 \times 10^{-5}$, $a_3 = 1.718 \times 10^{-4}$, $b_3 = 7.814 \times 10^{-5}$, $a_4 = 7.440 \times 10^{-5}$, $b_4 = 5.304 \times 10^{-5}$, $a_5 = 1.305 \times 10^{-4}$, $b_5 = -1.464 \times 10^{-5}$, $w = 5.848$.

Based on the fitting curve obtained from the experiment, the accuracy calculation of the eye tracking system can be carried out. The residual value at each angular value is obtained from the fitting curve and the actual measured peak interval, and then the standard deviation is obtained, which can be used to represent the accuracy estimation of the system. The smaller the value of standard deviation, the higher the accuracy of the eye tracking system. The formula for calculating the standard deviation is:

$$\sigma = \sqrt{\frac{\sum_{i=1}^{n} v_i^2}{n-t}} \tag{13}$$

where n is the number of data points collected, vi denotes the residual obtained from each data point, and is the number of unknown quantities in the fitting expression. By calculation, the standard deviation σ of the experimental data is obtained as 0.0002663 ms. full differentiation of the previous equation gives the functional systematic error equation:

$$\begin{aligned} \Delta\theta_1 &= \frac{\Delta d_1}{d_2 \cdot \left(\frac{d_1^2}{d_2^2} + 1\right)} - \frac{\theta_m \cdot \Delta_{\Delta t} \cdot \cos\left(\frac{\Delta t}{2} - \frac{\omega \cdot T}{4}\right)}{2} \\ &- \frac{d_1 \cdot \Delta d_2}{d_1^2 + d_2^2} \end{aligned} \tag{14}$$

According to the calculation and analysis of the experiment, we can get that the corresponding values of the values in the measurement range are all less than 0.1°. Through the analysis, it can be seen that the peak interval error brings the error value of eye movement angle measurement less than 0.1°. From this, it can be concluded that the accuracy of the eye tracking system designed in this study is higher than 1°, which meets the design requirements.

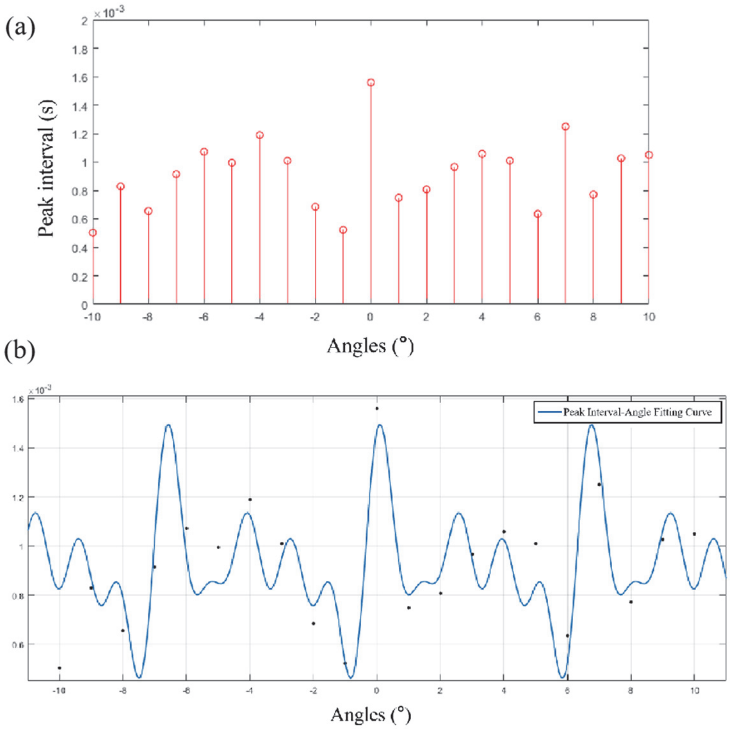

Figure 9 Variation of peak interval with angle change and fitting calculation (a) peak interval information obtained by intercepting multiple periodic signals and processing them; (b) peak interval-angle fitting curve

4 CONCLUSION

This study innovates on the traditional electrostatic micro-mirror comb structure by designing a slanted comb structure. Numerical calculations analyze the deflection angles of ordinary comb structures, serpentine comb structures, and slanted comb structures. The results indicate that the deflection displacement of the slanted comb mirror exceeds that of the ordinary comb mirror, demonstrating that the arrangement of the slanted combs enhances the deflection angle driven by the planar combs. Moreover, compared to ordinary comb-driven mirrors, the slanted comb-driven mirror exhibits a greater deflection angle. By combining theoretical and experimental approaches, a novel eye-tracking discrimination method is proposed. This method utilizes the resonant characteristics of MEMS mirrors and identifies an optimal driving signal frequency of 1050 Hz to ensure the scanning range closely matches the size of the eye's surface. The experiment captures original eye movement information by analyzing the voltage signal characteristics collected by the photodiode when the eye is in different positions. The experiment reveals that the signals obtained when the eye rotates left and right are essentially symmetrical around the 0° position, exhibiting fluctuations influenced by trigonometric functions, and successfully derives a fitting expression. Validation shows that the eye-tracking accuracy of the experimental system is better than 1°. Thus, the eye-tracking scanning determination method based on MEMS mirrors explored in this research is proven to be feasible, and the constructed experimental system meets accuracy requirements. However, the eye tracking discrimination method proposed in this paper relies on the coordinate correction between the MEMS micromirror relative to the eye when it is used in practice, and real-time calibration algorithms based on artificial intelligence can be used to improve the performance in the future, and at the same time, the combination of algorithms and hardware based on artificial intelligence and MEMS micromirrors is also a future research focus of eye tracking.

5 REFERENCES

[1] Wang, X., Cai, F., & Liu, F. (2015). Non-contact dynamic real-time eye tracking technology. *Journal of Frontiers of Computer Science and Technology*, *9*(3), 266-78.

[2] Bhakta, V., Kalinowski, D, A., & Choi, H. (2024). Optical systems with lens-based static foveation: U.S. Patent 11, 867, 907.

[3] Chen, Z., Fu, H., Lo, W-L., & Chi, Z. (2018). Strabismus Recognition Using Eye-Tracking Data and Convolutional Neural Networks. *Journal of Healthcare Engineering*, *2018*, 1-9. https://doi.org/10.1155/2018/7692198

[4] Wygnaski-Jaff, T., Kushne, B, J., Moshkovit, A. et al. (2023). An Eye-Tracking - Based Dichoptic Home Treatment for Amblyopia. *Ophthalmology*, *130*(3), 274-85. https://doi.org/10.1016/j.ophtha.2022.10.020

[5] Tadokor, K., Yamashit, T., Fukui, Y. et al. (2021). Early detection of cognitive decline in mild cognitive impairment and Alzheimer's disease with a novel eye tracking test. *Journal of the Neurological Sciences*, *427*. https://doi.org/10.1016/j.jns.2021.117529

[6] Holmqvist, K., Nyström, M., Andersson, R. et al. (2011). *Eye tracking: A comprehensive guide to methods and measures*. OUP Oxford.

[7] Pu, C., Park, S., Chu, P, B. et al. (2004). Electrostatic actuation of three-dimensional MEMS mirrors using sidewall electrodes. *IEEE Journal of Selected Topics in Quantum Electronics*, *10*(3), 472-477. https://doi.org/10.1109/JSTQE.2004.828480

[8] Gu-Stoppel, S., Lisec, T., Fichtner, S. et al. (2019). A highly linear piezoelectric quasi-static MEMS mirror with mechanical tilt angles of larger than 10. *MOEMS and Miniaturized Systems XVIII. SPIE*, *10931*, 1093102. https://doi.org/10.1117/12.2509577

[9] Zhang, X., Zhou, L., & Xie, H. (2015).A fast, large-stroke electrothermal MEMS mirror based on Cu/W bimorph. *Micromachines*, *6*(12), 1876-1889. https://doi.org/10.3390/mi6121460

[10] Bernstein, J., Taylor, W, P., Brazzle, J. et al. (2003). Two axis-of-rotation mirror array using electromagnetic MEMS. *The Sixteenth Annual International Conference on Micro Electro Mechanical Systems. MEMS-03 Kyoto. IEEE*, *2003*, 275-278. https://doi.org/10.1109/MEMSYS.2003.1189739

[11] Solgaard, O., Godil, A, Howe, A. et al. (2014). Optical MEMS: From micromirrors to complex systems. Journal of *Microelectromechanical systems*, *23*(3), 517-538. https://doi.org/10.1109/JMEMS.2014.2319266

[12] He, S., Mrad, R, B., & Chong, J. (2011). Repulsive-force out-of-plane large stroke translation micro electrostatic actuator. *Journal of Micromechanics and Microengineering*, *21*(7), 075002. https://doi.org/10.1088/0960-1317/21/7/075002

[13] Ko, Y.-C., Cho, J.-W., Mun, Y.-K. et al. (2005). Eye-type scanning mirror with dual vertical combs for laser display. *Sensors & Actuators: A. Physical*, *126*(1), 218-226. https://doi.org/10.1016/j.sna.2005.10.013

[14] Milanovic, V., Castelino, K., & McCormick, D. T. (2007) Highly adaptable MEMS-based display with wide projection angle. *2007 IEEE 20th International Conference on Micro Electro Mechanical Systems (MEMS), IEEE*, 143-146. https://doi.org/10.1109/MEMSYS.2007.4433036

[15] Liu, Y., Yuan, W., Qiao, D. et al. (2013). A two-dimensional high-frequency electrostatic microscanner. *Chinese Optics Letters*, *11*(11), 112302. https://doi.org/10.3788/COL201311.112302

[16] Tatler, B. W., Wade, N. J., Kwan, H., Findlay, J. M., & Velichkovsky, B. M. (2010). Yarbus, Eye Movements, and Vision. *i-Perception*, *1*(1), 7-27. https://doi.org/10.1068/i0382

[17] Li, Y., Wang, S., & Ding, X. (2010). Eye/eyes tracking based on a unified deformable template and particle filtering. *Pattern Recognition Letters*, *31*(11), 1377-87. https://doi.org/10.1016/j.patrec.2010.02.013

[18] Zhang, J., Wu, Y., Huang, H., & Hou, G. (2018). A New Human Eye Tracking Method Based on Tracking Module Feedback TLD Algorithm. *2018 IEEE 20th International Conference on High Performance Computing and Communications.* https://doi.org/10.1109/HPCC/SmartCity/DSS.2018.00071

[19] Yamamoto, S. & Moshnyaga, V. G. (2009). Algorithm Optimizations for Low-Complexity Eye Tracking. *Proceedings of the 2009 IEEE International Conference on Systems, Man, and Cybernetics*. https://doi.org/10.1109/ICSMC.2009.5346389

[20] Amudha, J. & Chandrika, K. R. (2016). Suitability of Genetic Algorithm and Particle Swarm Optimization for Eye Tracking System. *2016 IEEE 6th International Conference on Advanced Computing (IACC).* https://doi.org/10.1109/IACC.2016.56

[21] Beymer, D. & Flickner, M. (2003). Eye gaze tracking using an active stereo head. *2003 IEEE Computer Society Conference on Computer Vision and Pattern Recognition, IEEE*, *2*, II-451. https://doi.org/10.1109/CVPR.2003.1211502

[22] Topal, C., Gerek, Ö, N., & Doğan, A. (2008). A head-mounted sensor-based eye tracking device: eye touch

system. *Proceedings of the 2008 symposium on Eye tracking research & applications*, 87-90. https://doi.org/10.1145/1344471.1344494

[23] Bobić, V. & Graovac, S. (2017). Simple and precise commercial camera based eye tracking methodology. *Telfor Journal*, *9*(1), 49-54.

[24] Okan, O., Suleyman, B., & Mehmet Umit, A. (2022). Evaluation of Vibration Signals Measured by 3-Axis MEMS Accelerometer on Human Face using Wavelet Transform and Classifications. *Tehnicki Vjesnik - Technical Gazette*, *29*(2). https://doi.org/10.17559/TV-20210820150837

[25] Ozdogan, M., Daeichin, M., Ramini, A., & Towfighian, S. (2017). Parametric resonance of a repulsive force MEMS electrostatic mirror. *Sensors and Actuators A: Physical*, *265*, 20-31. https://doi.org/10.1016/j.sna.2017.07.043

YanTing XIA
School of Electronic Information Engineering,
Geely University of China, Chengdu, 641423

Qian WANG
School of Electronic Information Engineering,
Geely University of China, Chengdu, 641423

Qitao LI
(Corresponding author)
Upper Changjiang River Bureau of Hydrological and Water Resources Survey,
Hydrology Bureau of Changjiang Water Resources Commission,
Chongqing, 400020
E-mail: liqitao@stu.cdut.edu.cn

Lin ZHANG
School of Electronic Information Engineering,
Geely University of China, Chengdu, 641423